

SDS-Assisted Hydrothermal Growth and Photocatalytic Activity of Like-Caviar MoFe_2O_4 Nanoparticle Decorated with Al_2O_3

Mohammed Ali Hameed and Luma Majeed Ahmed*

Department of Chemistry, College of Science, University of Kerbala, Kerbala 56001, Iraq

* **Corresponding author:**

tel: +964-7801683055

email: luma.ahmed@uokerbala.edu.iq

Received: August 29, 2023

Accepted: October 2, 2023

DOI: 10.22146/ijc.88444

Abstract: Like-caviar molybdenum ferrite nanoparticles (MoFe_2O_4 NPs) have been successfully synthesized via a hydrothermal route in the presence of the negative surfactant (sodium dodecyl sulfate (SDS)). SDS acts as a template, stabilizer, and stops the aggregating process through storage. The mean crystal size of MoFe_2O_4 NPs rises with decorating it with Al_2O_3 . Based on SEM analysis, the shapes of MoFe_2O_4 , Al_2O_3 , and their composite demonstrated like-caviar, like-brain cells, and like-grains, respectively. Al_2O_3 has been chosen to incorporate with spinel MoFe_2O_4 to make it color more light, this crucial step is necessary to enhance their optical characteristics. FTIR spectra observed the MoFe_2O_4 NPs are inverse spinel. The photo-decolorization test employs indigo carmine (IC) as a model pollutant. The quantum yields (Φ) of IC dye decolorization with studied photocatalysts are low, which may be created by quencher materials, dimerization of dye molecules, and photophysical deactivation processes (ISC process). Moreover, the photocatalytic activity of using MoFe_2O_4 raised after being decorated with alumina, which revealed an increase in the surface acidity, hydroxyl group adsorption, size, band gap, pH_{pzc} of MoFe_2O_4 from 2.9–3.6 to 4.2–5.9 after decorated alumina. This pH is suitable for decolorizing IC dye, which has a pH of solution equal to 5.3.

Keywords: Molybdenum ferrite nanoparticle; hydrothermal synthesis; zero point charge (pH_{pzc}); indigo carmine dye; quantum yields

■ INTRODUCTION

The usage of photocatalysts in alcoholic or aqueous solutions has expanded due to growing applications in many spheres of human existence [1]. The production of reactive oxygen species (ROS), including superoxide anion, hydrogen peroxide, and the hydroxyl radical, under artificial or solar light illumination is essential for the photocatalyst to function [2]. One of the potential effluent treatment methods is the photocatalytic process, which can decompose or eliminate organic hazardous contaminants in an environmentally acceptable manner [3-4]. As a result, researchers are working to create new and highly effective photocatalysts to combat the problems associated with water pollution [5-7]. Due to the fact that visible light radiation accounts for half of all solar energy absorbed by the planet, semiconductor photocatalysts, particularly those driven by visible light, have drawn significant attention [8]. Due to the toxicity and danger of

dyes, it is highly desirable to design and implement high-efficiency, low-cost, and stable photocatalysts driven by visible light for practical application. There are many ways to remove dyes from wastewater, including adsorption, photocatalysis, photodegradation, membrane filtration, oxidation, and irradiation [9]. In order to enable the recovery of valuable compounds, it is crucial to create effective adsorbents that demonstrate superior performance in their ability to remove pollutants and possess suitable properties, such as ease of separation from the solution, regeneration, and efficiency, even after multiple cycles of use.

Metal oxides have been investigated recently as possible materials with various properties [10]. One of the most promising classes of mixed metal oxides, which have recently been the subject of intense research, is the family of metal molybdates [11]. Because they have significant industrial applications, metal molybdate

compounds with the formula $M\text{MoO}_4$ or $M_2(\text{MoO}_4)_3$ are significant inorganic materials that have generated a lot of research interest. These include optical fibers, photoluminescent compounds, humidity sensors, scintillator materials, and photocatalytic materials [12]. Molybdenum ferrite (MoFe_2O_4) is probably the most researched of all the mixed oxides that contain molybdenum. It has attracted a steadily growing amount of interest, has been synthesized at the nanoscale using various techniques, and has been used in numerous commercial and environmental applications [13]. MoFe_2O_4 , a significant n-type binary metal oxide semiconductor, exhibits outstanding redox properties, catalytic activity, and chemical stability because of the modulation between octahedral (FeO_6) and tetrahedral (MoO_4) [14]. The balance between in the octahedral and tetrahedral sites may serve as a proxy for the valence distribution [15]. MoFe_2O_4 has significant industrial uses as a catalyst [11].

Several synthesis methods were proposed for the production of MoFe_2O_4 , including precipitation [16], solvothermal [17], microwave [18], and hydrothermal methods [19]. Among the above methods, a hydrothermal method has many advantages, such as shorter reaction time, more informed product dimensions and composition, and ease of tuning compositions of the products [20]. Furthermore, this method is very easy to use and reasonably priced for creating functional materials in the nanometer range [21]. One of the best matrices for introducing metallic nanoparticles and well-liked oxide supports for metal catalysts is alumina. Alumina films and coatings offer great transparency, a wide surface area, a narrow band gap, and excellent thermal, chemical, corrosion, and radiation resistance. As a result, alumina films are frequently utilized in membrane technology, optoelectronics, aerospace, microelectronic devices as gate insulators, sensors as an antireflective coating, and catalysis [22]. Recently, aluminum oxide can be used as a support material to increase the surface area and therefore its activity of the metal catalyst. The choice of the appropriate support is therefore a very significant issue because the support material is effective in the surface of the active phase contribution in catalytic reaction [23].

The goal of this work is focused on the synthesis of MoFe_2O_4 nanoparticles at a low temperature via a relatively cost-effective and very simple procedure in the presence of negative surfactant as a template. The proposes of MoFe_2O_4 synthesis using a hydrothermal synthesis supported by a negative surfactant as a template to become more stable and then incorporation with commercial Al_2O_3 as a nanocomposite using ultrasonic technique. The structure, morphology, and optical properties of the MoFe_2O_4 NPs, Al_2O_3 , and $\text{MoFe}_2\text{O}_4/\text{Al}_2\text{O}_3$ nanocomposite were investigated. The photocatalysis activity of these samples has been applied by determining the photo-decolorization efficiency (PDE%) and quantum yields (Φ).

■ EXPERIMENTAL SECTION

Materials

The powdered ferric nitrate nonahydrate ($\text{Fe}(\text{NO}_3)_3 \cdot 9\text{H}_2\text{O}$), commercial Al_2O_3 (Switzerland company) and sodium molybdate dihydrate ($\text{Na}_2\text{MoO}_4 \cdot 2\text{H}_2\text{O}$) were purchased by Sigma Chem Co. USA. Hydrochloric Acid (35%) was supplied from a general drug house. Absolute ethanol ($\text{C}_2\text{H}_5\text{OH}$) was purchased by BDH. The sodium dodecyl sulfate (SDS) was provided by Qualikems, DIDACTIC. The dye indigo carmine ($\text{C}_{16}\text{H}_8\text{N}_2\text{Na}_2\text{O}_8\text{S}_2$) was purchased by Sigma-Aldrich Chemie. This dye is acidic type, molar mass of 466.36 g/mol, λ_{max} of 600 nm and the structure as Fig. 1. They were used as received without further purification.

Instrumentation

The produced samples were characterized using the Shimadzu Lab X-XRD 6000 X-ray diffraction spectroscopy, Kyky's EM-320 scanning electron microscopy with energy dispersive X-ray spectroscopy,

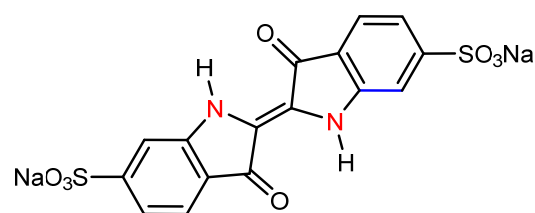


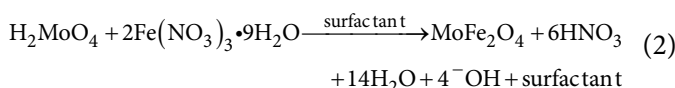
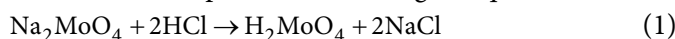
Fig 1. The structure of a dye Indigo Carmine (IC)

Shimadzu's 8400S FTIR spectrometers, and Shimadzu's 1800 UV-visible spectrophotometer. Simple instruments were used for the preparation and application phases, including a sensitive balance (Sartorius, BL 210 S), a pH meter (OAICTON-2100), an ultrasonic (DAIHAN Scientific), a magnetic stirrer (Heido-MrHei-Standard), a centrifuge (Hettich-Universal II), and a furnace (Muffle furnace Size-Tow Gallenkamp). The hydrothermal process was utilized (steel with white Teflon tube autoclave type TOPT-HP100 TOPTION), and the ultraviolet lamp (HPML, 400 W, Radium) was used as a key component in a homemade photo-reactor were some of the additional instruments that were used for this project.

Procedure

Preparation of MoFe_2O_4 in the presence of SDS-surfactant

MoFe_2O_4 like caviar was prepared using the hydrothermal method. In a typical synthesis, 35 mL of distilled water was used to dissolve 2.828 g of $\text{Fe}(\text{NO}_3)_3 \cdot 9\text{H}_2\text{O}$, while 25 mL of distilled water and 10 mL of HCl were used to dissolve 0.846 g of $\text{Na}_2\text{MoO}_4 \cdot 2\text{H}_2\text{O}$ [21] at room temperature according to Eq. (1) and (2):



The $\text{Fe}(\text{NO}_3)_3$ solution was vigorously stirred before the Na_2MoO_4 solution was added, this is in agreement with described in the literature [19]. After that, 0.5 g of SDS surfactant was added to the solution as a template and stabilizer. The resulting yellow slurry was stirred for 15 min before being placed in a 100 mL teflon-lined autoclave. After that, the autoclave was sealed and kept in the oven at 180 °C for 5 h. The autoclave was then cooled for 2 h to room temperature. Following filtration, the obtained solid sample was repeatedly washed with distilled water and then ethanol to ensure that all precursor salt-positive ions and humidity were eliminated. This precipitate was placed inside a desiccator overnight to gently dry using silica gel. The dried precipitate was ground to a homogeneous powder to produce the final MoFe_2O_4 sample. This method was modified from the reported procedure [24].

However, Fig. 2 shows the proposed method for utilizing a surfactant during the production of molybdenum ferrite. The step of adding the surfactant during the hydrothermal technique is essential because it acts as a stabilizer agent and a template at the same time, preventing the hydrolysis of metal by water and ensuring that MoFe_2O_4 NPs morphology develops uniformly. Additionally, the surfactant is crucial to ensuring that the produced nanocomposite is stabilized during the storage procedure.

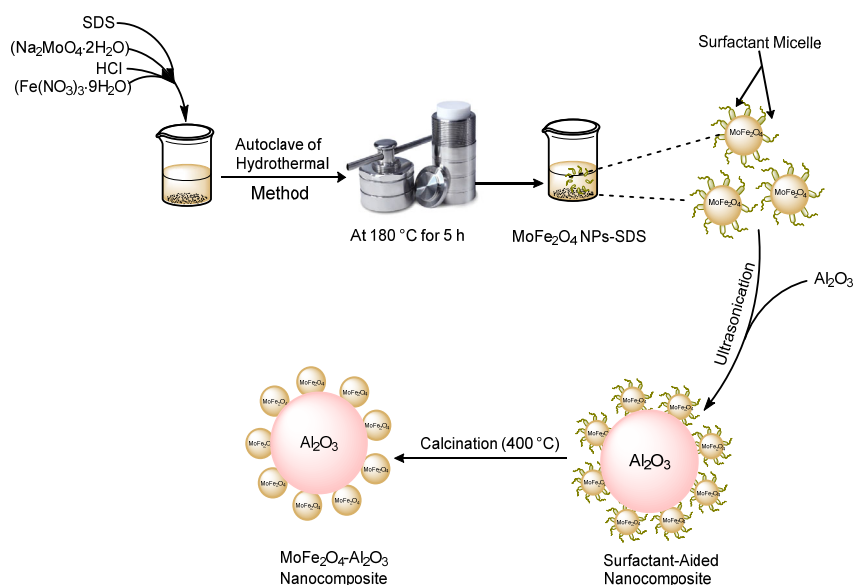
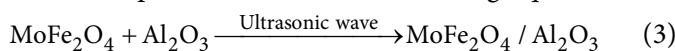


Fig 2. Schematic of surfactant-aided MoFe_2O_4 NPs and nanocomposite [24-25]

Preparation of MoFe₂O₄/Al₂O₃ nanocomposite

The MoFe₂O₄:Al₂O₃ nanocomposite was created in a 1:2 ratio utilizing an ultrasonic wave. Both the MoFe₂O₄ and Al₂O₃ solutions were dispersed for 2 h at 75 °C using ultrasonic waves at a frequency of 65 kHz. To accomplish the binding process between MoFe₂O₄ and Al₂O₃, the MoFe₂O₄ in the presence of SDS-surfactant solution was gradually added to the Al₂O₃ solution over the course of 2 h at 75 °C; this procedure is similar and in agreement with the reported in the literature [26]. The light brown precipitate was filtered and washed with water and ethanol, then stored overnight in a desiccator. The recommended chemical equation for the interaction of MoFe₂O₄ with Al₂O₃ nanoparticles was determined using Eq. (3).



Determination of zero-point charge (pH_{ZPC})

Titration was carried out using 0.3 g of prepared photocatalyst samples powder with 100 mL from three different ionic strength solutions (0.001, 0.010, and 0.100 M KCl). The solution by N₂ was purged into the system to expel CO₂ contamination for 30 min. The initial pH was determined using a pH meter before addition. The KOH titrant solution was used to carry out the titration by adding 1 mL every 3 min, using the three ionic strength solutions (0.100, 0.010, and 0.001 M) in the presence of the photocatalysts prepared separately. The values of the change in the pH after using these solutions were measured. The process of adding the KOH is repeated until the change in the pH value is stable. After the completion of the titration process, the point of zero charge (PZC) was determined by locating the common point of intersection of the titration ionic strength curves at different pH [27].

Photo-decolorization of IC dye using MoFe₂O₄, Al₂O₃ and MoFe₂O₄/Al₂O₃ nanocomposite

The MoFe₂O₄ in the presence of SDS as a negative surfactant, Al₂O₃ and MoFe₂O₄/Al₂O₃ nanocomposite act as photocatalysts and are utilized in the decolorization of IC dye. The photoreaction was applied using a homemade photoreactor in Fig. 3. This photoreactor includes 400 watts Philips UV-A lamp with a light intensity equal to 2.95×10^{-7} Einstein s⁻¹; the body of the reactor is manufactured from a wooden box covered with aluminum

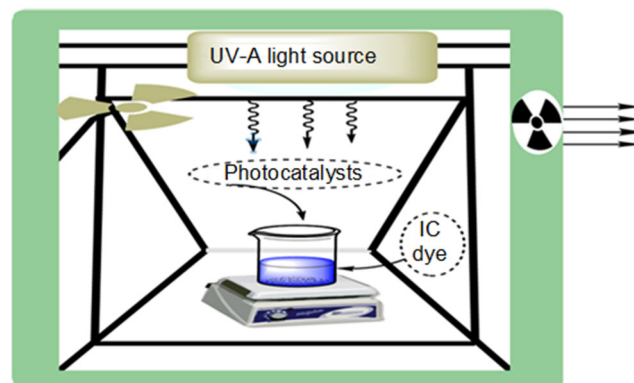


Fig 3. Diagrammatic representation of a homemade photocatalytic reactor unit

foil to prevent hazards light and focused at the light in the same time. This wooden box contains an inside magnetic stirrer, Pyrex glass beaker (500 mL), a teflon bar, and two various fans to depress and fix the temperature [28].

At different temperatures (10, 15, 20, and 25 °C) and with an initial pH of 5.3, exactly 0.1 g of all photocatalyst samples were mixed with 25 ppm of IC dye. The generated suspension solution was magnetically agitated for 15 min without irradiation to enable the attainment of equilibrium adsorption [29-30]. After the adsorption step, UV light was applied to this suspension, and then about 3 mL aliquots were collected at irradiation intervals of up to 100 min (every 10 min 3 mL was withdrawn). The collected suspensions were separated twice at 5,000 rpm for 20 min, and the adsorption of the produced filters was recorded at 600 nm using UV-visible spectroscopy. The photo-decolorization efficiency percentage (PDE%) [31] was determined in Eq. (4) depending on the initial concentration of dye (C₀) at the adsorption process (mg/L), and residue dye concentration (C_t) under irradiation (mg/L).

$$\text{PDE (\%)} = \frac{(C_0 - C_t)}{C_0} \times 100 \quad (4)$$

RESULTS AND DISCUSSION

FTIR Analysis

In order to analyze the surface structure and gain an understanding of chemical bonds, the FTIR analysis was performed. The measured spectral span ranged

from 250 to 4000 cm^{-1} . The FTIR spectra of MoFe_2O_4 in the presence of SDS-surfactant, Al_2O_3 , and $\text{MoFe}_2\text{O}_4/\text{Al}_2\text{O}_3$ nanocomposite are shown in Fig. 4. The MoFe_2O_4 in the presence of SDS-surfactant NPs has a good ability to expand the O–H band, the characteristic band at 3429.5 cm^{-1} can be attributed to them. The tetrahedral species of Mo are stretching and exhibit broad bands at 837.1 and 1114.8 cm^{-1} , which coupling bond between oxygen and molybdenum. The broad vibration bands from 582.2 to 837.1 cm^{-1} are attributed to the Mo–O–Mo bridge and the Mo=O terminal stretch. The weak bands obtained at 456.4–486.8 cm^{-1} can be attributed to Fe–O–Mo stretching vibration as in references [32]. The characteristic bands of the Al–O vibration were occurred at 435.9, 582.5, and 1624.1 cm^{-1} [33]. The Mo–O asymmetrical stretching band was observed around 509.2 cm^{-1} , while the weak band obtained at 478.3 cm^{-1} can be attributed to Fe–O and Al–O stretching vibration modes [34]. The band of Fe–Al–O at 648.6 cm^{-1} was also observed [35].

Structural Properties

The photocatalyst samples prepared with SDS as a surfactant were described as MoFe_2O_4 in the presence of SDS-surfactant, Al_2O_3 , and $\text{MoFe}_2\text{O}_4/\text{Al}_2\text{O}_3$ nanocomposite, respectively. The XRD spectra of the photocatalyst samples are shown in Fig. 5. The three samples show the different diffraction characteristics clearly explain the appearance of several patterns related to its basic components, where the presence of peaks located at 14.127°, 15.403°, 16.554°, 19.589°, 20.541°, 21.851°, 22.966°, 25.806°, 27.579°, 30.288°, and 34.118° which are attributed to the indexed plants (210), (003), (020), (312), (311), (022), (202), (022), (212), (122), and (042), respectively, proving the formation of MoFe_2O_4 and can be well-indexed to monoclinic structure of MoFe_2O_4 , these results are in line with (JCPDS card No. 83-1701) [19]. The high intensities of the XRD patterns suggested that the sample is highly crystalline. No other diffraction peaks were observed, which shows the high purity of the as-prepared MoFe_2O_4 in the SDS surfactant. The Al_2O_3 phase is supported by the observed diffraction peaks at 25.606°, 35.176°, 37.799°, 43.377°, 52.567°, 57.516°, and 68.221°, which are connected to the (311),

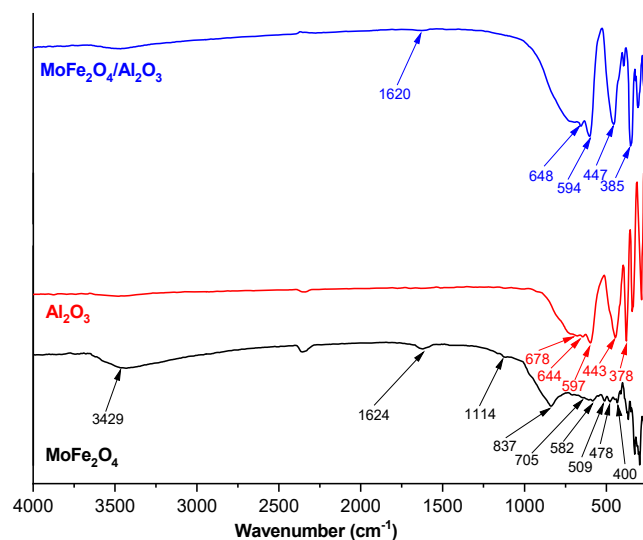


Fig 4. FTIR spectra of MoFe_2O_4 in the presence of the SDS-surfactant, Al_2O_3 , and $\text{MoFe}_2\text{O}_4/\text{Al}_2\text{O}_3$ nanocomposite

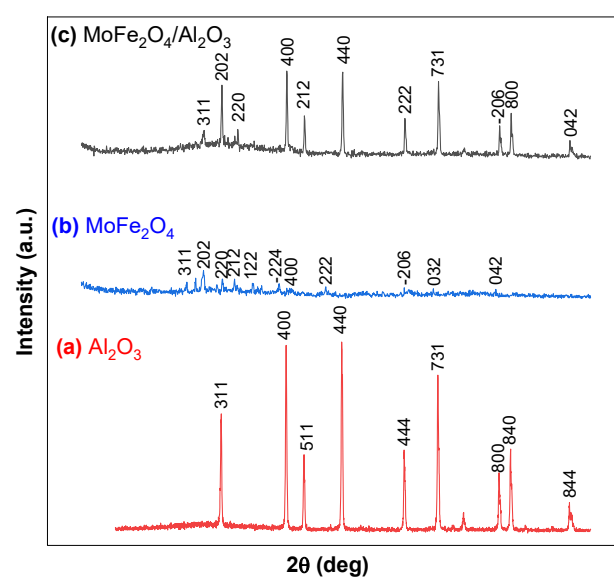


Fig 5. XRD pattern of (a) Al_2O_3 , (b) MoFe_2O_4 in the presence of SDS-surfactant, and (c) $\text{MoFe}_2\text{O}_4/\text{Al}_2\text{O}_3$ prepared in the presence of the SDS

(400), (511), (440), (444), (731), and (840) reflections, respectively. The samples' whole range of diffraction peaks agrees with the data from data (JCPDS card 10-0425) [36]. When the MoFe_2O_4 and Al_2O_3 incorporate as a nanocomposite, some essential peaks in Al_2O_3 are shifted toward the high 2θ such as 25.606°, 35.176° and 43.377° are shifted to 25.724°, 35.282° and 43.486°, respectively, that proved the formation of

nanocomposite and the alumina is a substrate of MoFe_2O_4 . The mean crystal sizes of the MoFe_2O_4 in the presence of SDS-surfactant, Al_2O_3 , and $\text{MoFe}_2\text{O}_4/\text{Al}_2\text{O}_3$ nanocomposite were calculated using the Scherrer formula [37-38], according to Eq. (5);

$$L = \frac{k\lambda}{\beta \cos \theta} \quad (5)$$

where, $k = 0.9$ (constant), $\lambda = 1.54 \text{ \AA}$, $\beta = \text{FWHM}$, $\theta = 2\theta/2$, L corresponds to the mean size of crystallite (nm).

The mean size of MoFe_2O_4 in the presence of SDS-surfactant was about 23.83 nm at (202), (022), and (212), while the sizes of Al_2O_3 at (400), (440), (731), and $\text{MoFe}_2\text{O}_4/\text{Al}_2\text{O}_3$ nanocomposite at (202), (440), and (731) were about 43.44 and 47.84 nm, respectively. The large size of the nanocomposite crystals is attributed to the successful combination between Al_2O_3 and MoFe_2O_4 in the presence of SDS surfactant.

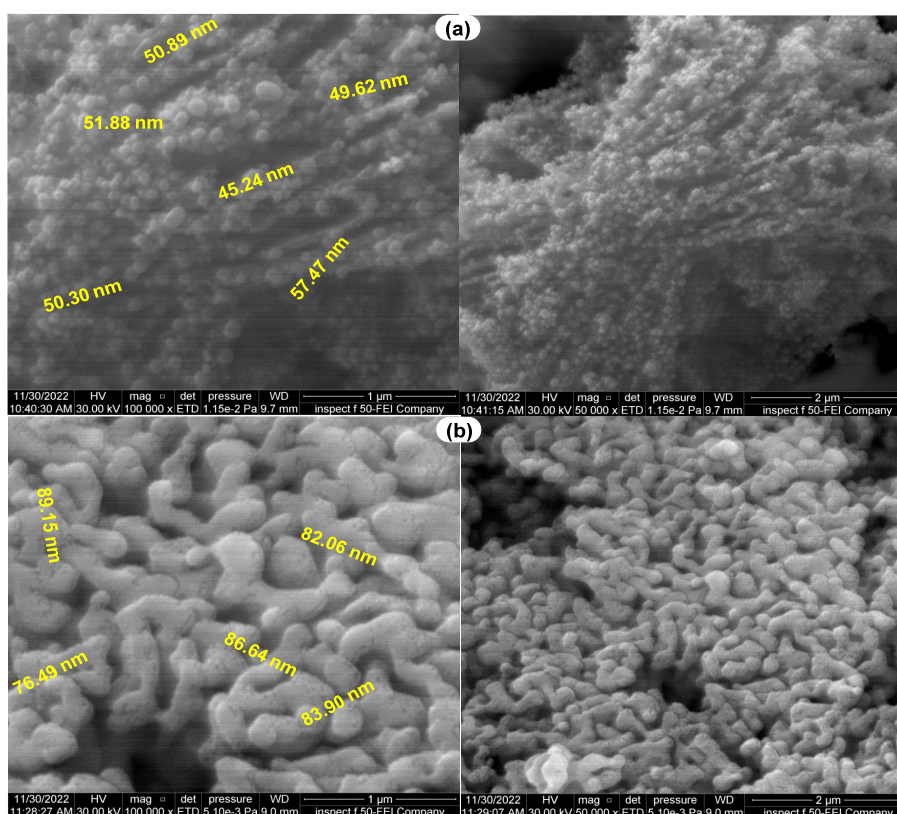
SEM Analysis

The morphologies and microstructures of the MoFe_2O_4 , Al_2O_3 and $\text{MoFe}_2\text{O}_4/\text{Al}_2\text{O}_3$ nanocomposite samples can be observed from SEM images (HR-SEM)

analysis. It can be clearly found that MoFe_2O_4 is composed of uniform spherical NPs like caviar with an average particle size of 50.9 nm, and the Al_2O_3 was a like-brain cell with average particle size of 83.64 nm, while when coupled, MoFe_2O_4 with Al_2O_3 , the shaped are appeared a highly agglomerated as a sub-micron sized particles with nanograin-like secondary particles on the surface, with the mean particle size 55.22 nm (Fig. 6(a-c)). Moreover, the high percentage of Al_2O_3 in comparison to spinel MoFe_2O_4 leads to a large size of nanocomposite.

EDX Analysis

By using EDX analysis, the elemental and percentage element compositions of the as-synthesized MoFe_2O_4 , commercial Al_2O_3 , and nanocomposite were validated. The results demonstrate that Fe, Mo, Al, and O are present in the elemental analysis in Fig. 7(a-c). They reveal that the photocatalyst sample contains 4.2 wt.% C, 34.3 wt.% O, 50.4 wt.% Fe, and 11.1 wt.% Mo for MoFe_2O_4 , Al_2O_3 contains 3.7 wt.% C, 48.4 wt.% O, and 47.8 wt.% Al, while $\text{MoFe}_2\text{O}_4/\text{Al}_2\text{O}_3$ nanocomposite



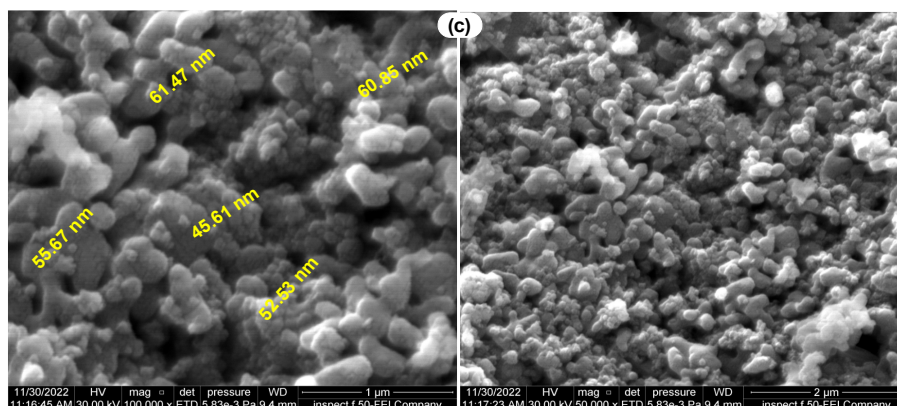


Fig 6. The SEM images of (a) MoFe_2O_4 in the presence of SDS-surfactant, (b) Al_2O_3 , and (c) $\text{MoFe}_2\text{O}_4/\text{Al}_2\text{O}_3$ nanocomposite in scale size 2 and 1 μm

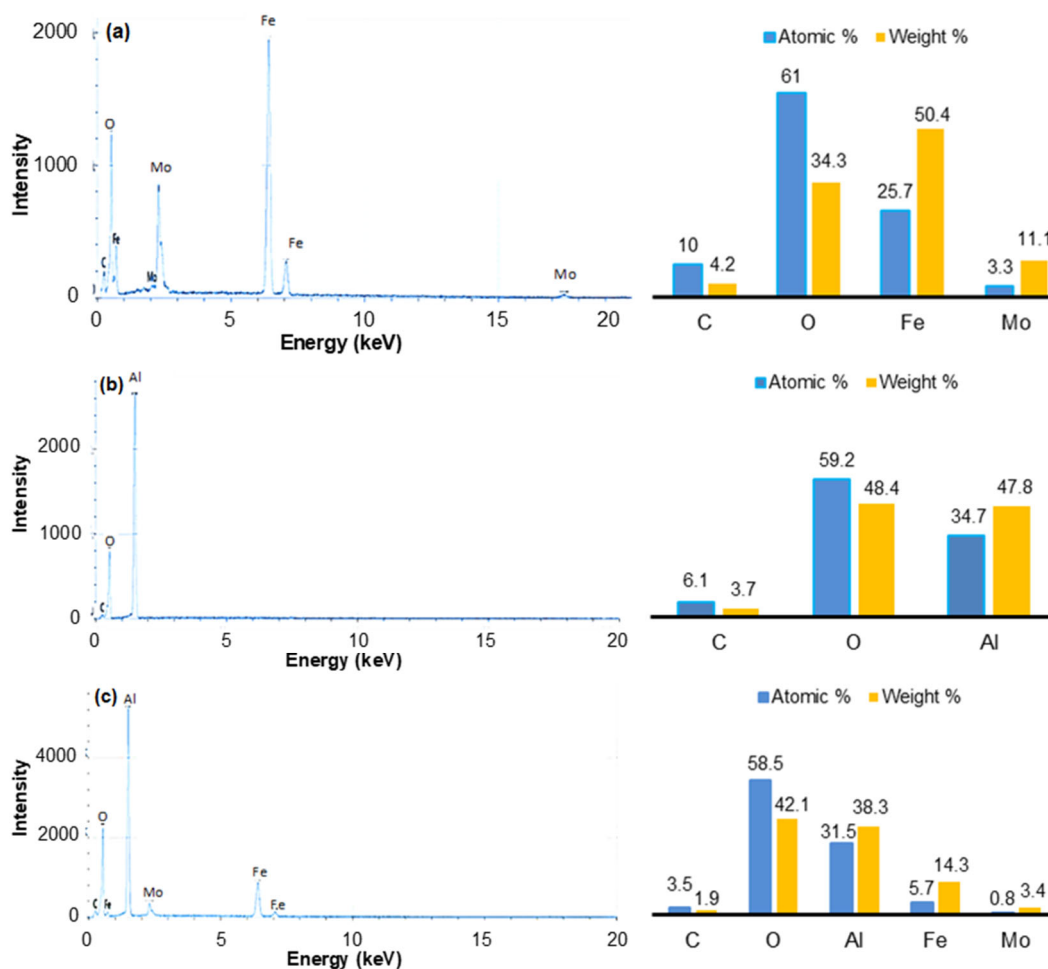


Fig 7. EDX spectra with a distribution of atomic % and weight % of (a) MoFe_2O_4 NPs in the presence of SDS-surfactant, (b) Al_2O_3 , and (c) $\text{MoFe}_2\text{O}_4/\text{Al}_2\text{O}_3$ nanocomposite

contains 1.9 wt.% C, 42.1 wt.% O, 14.3 wt.% Fe, 3.4 wt.% Mo, and 38.3 wt.% Al. The values are mostly determined by the ratio of each reactive substance, and this

composition also facilitates the synthesis of MoFe_2O_4 in the presence SDS-surfactant. That demonstrated that MoFe_2O_4 and the impurity-free $\text{MoFe}_2\text{O}_4/\text{Al}_2\text{O}_3$

nanocomposite (C is a substrate) were formed [17]. The Mo, Fe, Al, and O signals are well-defined, showing the active processing of metal oxides involving iron, molybdenum, and aluminum. With the stoichiometry preparation ratio 2:1 employed in the preparation technique, the Al peak strength for the samples prepared using higher Al precursor ratios has improved.

Optical Properties of Studied Photocatalysts

In the plotted Tauc equation in Fig. 8, the material's potential as a photocatalyst was determined by the optical energy bandgaps' (E_g) value in eV [39]. The Tauc equations (Eq. (6) and (7)) may be used to calculate the bandgap for all photocatalyst samples [40];

$$(\alpha h\nu)^{1/m} = k(h\nu - E_g) \quad (6)$$

$$\alpha = (2.3026A)/t \quad (7)$$

where h , α , ν , k , t , A , and m , are the Plank constant of the light, absorption coefficient, frequency, optical constant, thickness, absorbance, and constant value equal to 2 or $\frac{1}{2}$ for direct and indirect transitions, respectively. The band gaps of MoFe_2O_4 in the presence of SDS-surfactant, commercial Al_2O_3 , and $\text{MoFe}_2\text{O}_4/\text{Al}_2\text{O}_3$ nanocomposite are found to be 2.92 (direct), 4.40 (indirect), and 3.45 (indirect) eV, respectively. The increase of the band gap of MoFe_2O_4 in the presence of SDS-surfactant after being

decorated with Al_2O_3 , leads to depressing the recombination process with an increase in the internal layers in the conductive band and an increase in the response of photoreaction.

Effect of ZPC on Decolorization Efficiency

The solution pH is a vital factor in photocatalytic decolorization because it influences the surface charge of the catalyst. The type of pollutant and pH_{pzc} are the two factors that have the biggest effects on the optimal pH. The pH_{pzc} , which refers to a situation when the surface is neutrally charged, is used to describe the point where the pH curve and the titration curve cross. Finding the point of zero of the nanocomposites is essential for figuring out how much photocatalysis is occurring at a specific pH [41].

The appropriate pH settings for the photo-decolorization process are estimated by the pH_{pzc} data. Since H^+ ions prefer to remain on surfaces at low pH rather than in solutions, MoFe_2O_4 is positively charged, a property that at low pH will readily adsorb anions. However, at high pH, H^+ ions prefer to be in solution rather than in the material, therefore, the negatively charged MoFe_2O_4 surface will readily adsorb cations [42-43]. Based on Fig. 9(a-c), the pH_{pzc} values 2.9–3.6, 3.6–6.0,

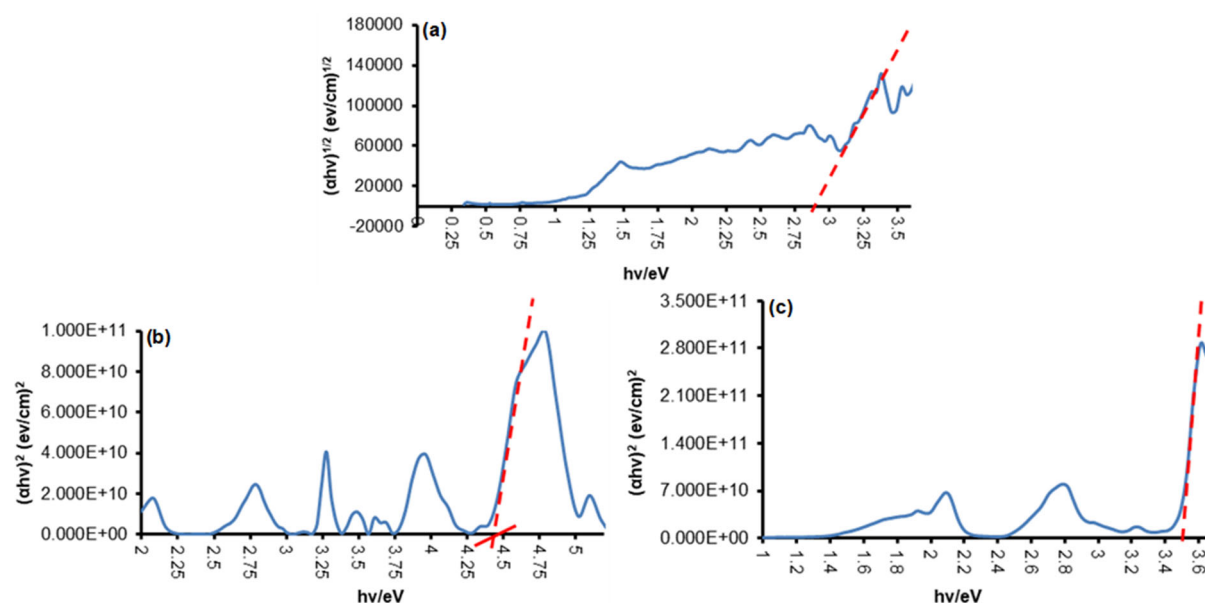


Fig 8. Tauc plot for (a) MoFe_2O_4 in the presence of SDS-surfactant as a direct band gap, (b) Commercial Al_2O_3 as an indirect bandgap and (c) for $\text{MoFe}_2\text{O}_4/\text{Al}_2\text{O}_3$ nanocomposite as an indirect bandgap

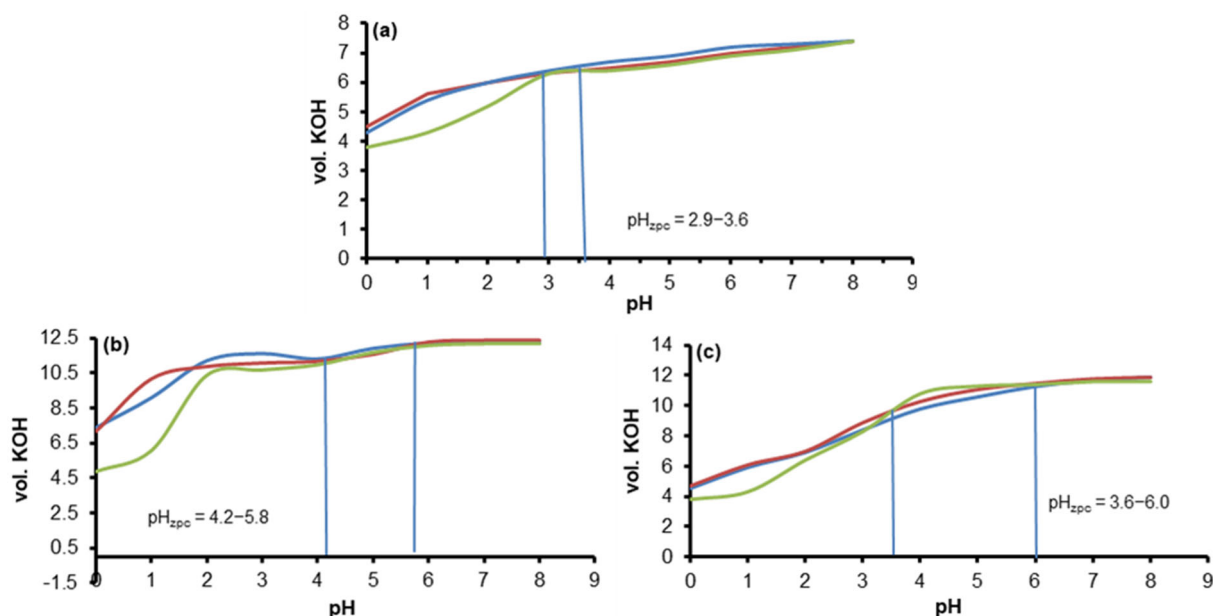


Fig 9. The point of zero charge (pH_{PZC}) of (a) MoFe_2O_4 , (b) Al_2O_3 , and (c) $\text{MoFe}_2\text{O}_4/\text{Al}_2\text{O}_3$ at different pH values, where using different concentration of KCl, brown line for 0.001 M, blue line for 0.010 M and green line for 0.100 M, respectively

and 4.2–5.8 are measured for MoFe_2O_4 , $\text{MoFe}_2\text{O}_4/\text{Al}_2\text{O}_3$, and Al_2O_3 , respectively. This result shows that MoFe_2O_4 and $\text{MoFe}_2\text{O}_4/\text{Al}_2\text{O}_3$ have a low pH_{pzc} , which allows them to quickly adsorb the IC dye (an anion dye) [44]. The pH_{pzc} value is used to determine an effective pH for photocatalytic decolorization. The optimum pH is dependent on the kind of pollution and pH_{pzc} . Specifically for IC as an anion dye, a pH value of 5.3 was found. This demonstrates that although anion dyes have a pH value of < 7 , which is acidic (+), any cation dyes have a pH value > 7 , which is alkaline (–) [26].

Photo-Decolorization of Indigo Carmine IC

The important significant factor in photo-catalytic activity is the properties and the nature of the used catalyst. It is important to understand why the catalytic activity of MoFe_2O_4 NPs in the presence of SDS-surfactant is evaluated after supporting in Al_2O_3 ; hence, a series of experiments were carried out with IC in aqueous suspension with the light of wavelength 600 nm [32,45], as shown in Fig. 10. The photocatalyst decolorization efficiency of $\text{MoFe}_2\text{O}_4/\text{Al}_2\text{O}_3$ nanocomposite is higher than that happened in the presence a pure MoFe_2O_4 NPs. This effect occurs because the band gap of MoFe_2O_4 is

smaller than that of Al_2O_3 , and it is a visible light active catalyst. It exhibits lower photocatalytic activity due to its lower valence band potential compared to Al_2O_3 [46]. That will improve the photocatalytic activity, though the charge carriers can migrate to MoFe_2O_4 due to the higher VB potential of Al_2O_3 . Moreover, this combined will elevate the acidity of the surface, which enhances the IC dye adsorption of the molecule over the catalyst surface and raises the generated hydroxyl radical, then direct attack of photogenerated holes [26,47].

Quantum yield of Photo-Decolorization of IC

The quantum yield is a measure of the photocatalytic reaction's efficiency and is based on how many molecules of the probe dye disintegrate for each photon that is absorbed [48]. The following equation may be used to determine the quantum yield (Φ) in the presence of a UV-A lamp, k_{app} is the apparent rate constant of the pseudo-first-order of the photo-decolorization of the dye in sec^{-1} [21,49], which is calculated using Eq. (8) and (9).

$$\ln\left(\frac{C_o}{C_t}\right) = k_{\text{app}} \times t \quad (8)$$

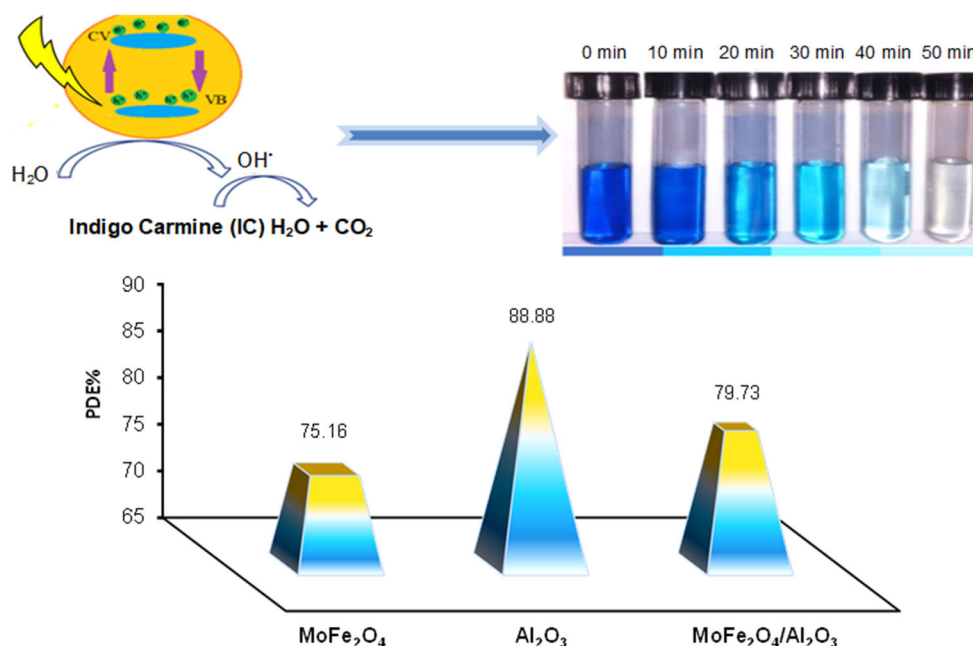


Fig 10. The relation of PDE% for IC dye decolorization in all samples photocatalyst solution for 50 min at 20 °C and pH = 5.3

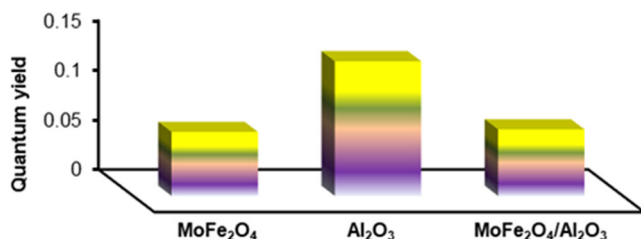


Fig 11. The relation of the quantum yield of IC dye photodecolorization with samples studied at pH 5.3 and temperature 20 °C

$$\Phi = \frac{k_{app}}{2.303I_0 \epsilon l} \quad (9)$$

Here: ϵ is the molar absorptivity of IC dye (84.469 mol⁻¹ L cm⁻¹), l is the path length term of the cell (cm), and I_0 is light intensity (3.195 × 10⁻⁷ Einstein s⁻¹) that calculated using chemical actinometrical method [50].

The quantum yield of IC dye decolorization is elevated as the following sequence: Φ using commercial Al₂O₃ > Φ using MoFe₂O₄/Al₂O₃ > Φ using MoFe₂O₄ NPs in the presence of SDS-surfactant, and equal to 0.135, 0.066, and 0.064, respectively, as in Fig. 11. These low Φ values are attitudes to may create quencher materials, a dimerization of dye molecules, and photophysical

deactivation processes (ISC process) as a result of recombination processes that trigger reversible reactions [51-52]. Where the Φ of MoFe₂O₄ NPs is low compared to its combination with Al₂O₃, as the efficiency ratio of the nanocomposite improved due to the separation of charges and the increase in surface acidity, which leads to the formation of ·OH for ·OH adsorption.

Suggested Decolorization Mechanism of IC

The products of the active species, such as superoxide anion, peroxide radical, and hydroxyl radical, in solution or on the surface of the photocatalyst are essential what determining any postulated mechanism for a photocatalytic process [53-54]. The ability of these species to dissolve and decolorize any organically colored materials has been changed. The hydroxyl radical works as a potent oxidant to damage the dye molecules because it is a more active species in an aqueous solution with 2.8 V [55-56]. Similar studies on the decolorization of IC propose that the isatin 5-sulfonic acid, the main aromatic component, was produced as a result of the C=C bond being broken by hydroxyl radicals attacking the compound's C₁ and C₁₀ positions. Oxidation of the two sulfonic groups in the starting molecule results in indigo,

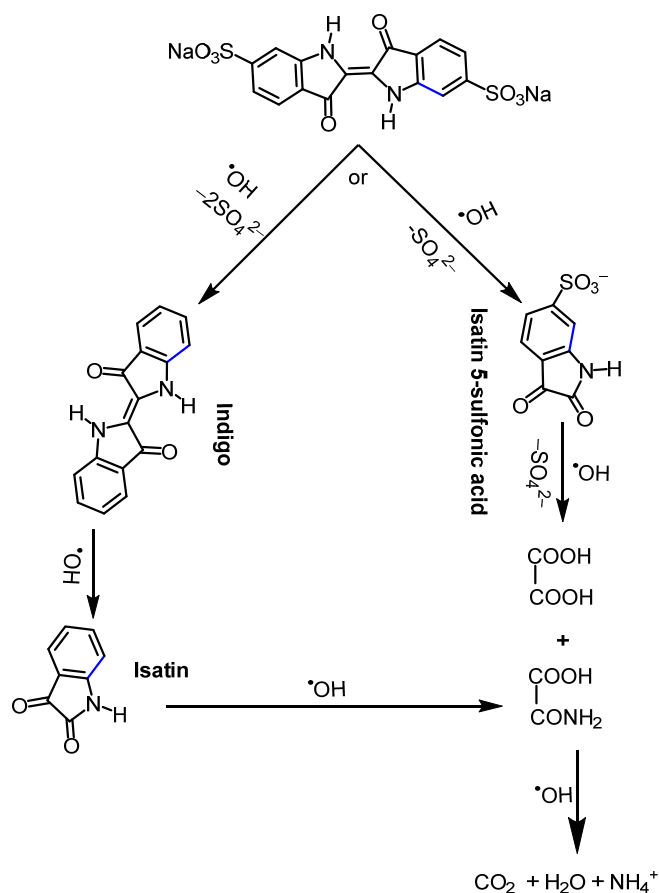


Fig 12. The schematic diagram for the decolorization and degradation process of the IC dye mediated by hydroxyl radicals in the photocatalytic system

which then undergoes the loss of two sulfonic groups to become isatin. Further decolorization of isatin 5-sulfonic acid, which also releases the sulfonic group and isatin, results in the production of oxalic and oxamic acid [57]. An almost complete mineralization is brought on by these carboxylic acids. Based on these observations, they applied the same degrading procedure as in Fig. 12 [58-59].

■ CONCLUSION

The hydrothermal technique was successfully used to prepare MoFe_2O_4 in the presence of SDS-surfactant. For the creation of structured MoFe_2O_4 is shaped like-caviar, the SDS vesicles can act as a template and stabilizer. The composite $\text{MoFe}_2\text{O}_4/\text{Al}_2\text{O}_3$ was prepared using ultrasonic waves, that is fast, environmentally friendly, and non-toxic. This nanocomposite has

appeared as a nano-grain. The FTIR spectra, which located the positions of the octahedral Mo–O and the tetrahedral Fe–O sites, demonstrated the formation of inverse spinel MoFe_2O_4 NPs. Using XRD analysis, the mean size of MoFe_2O_4 NPs was about 23.83 nm, while the size of Al_2O_3 and $\text{MoFe}_2\text{O}_4/\text{Al}_2\text{O}_3$ NCs was about 43.44 and 47.84 nm, respectively. The increase in the size of the NCs crystals is attributed to the successful combination of Al_2O_3 with MoFe_2O_4 . The SEM-EDX analysis and the samples prepared are confirmed. Additionally, the acidity of MoFe_2O_4 NPs surface elevated via incorporation with Al_2O_3 and caused the increase in catalytic activity from 75.16 to 79.73% at 50 min, which depended on an increase in generated electron-hole pairs that lead to hydroxyl radical in aqueous solution, as increase quantum yield of IC dye decolorization.

■ ACKNOWLEDGMENTS

The authors would like to thank everyone who helped with this paper from the scientific faculty at the University of Kerbala's Department of Chemistry.

■ AUTHOR CONTRIBUTIONS

The experiment was carried out by Mohammed Ali Hameed, and calculations for the k_{app} , quantum yield, PDE%, mean crystal size and band gaps were done by Mohammed Ali Hameed and Luma Majeed Ahmed. This manuscript was written by Mohammed Ali Hameed and Luma Majeed Ahmed. This manuscript's final version was approved by all authors.

■ REFERENCES

- [1] Collin, F., 2019, Chemical basis of reactive oxygen species reactivity and involvement in neurodegenerative diseases, *Int. J. Mol. Sci.*, 20 (10), 2407.
- [2] Ahmed, L.M., 2021, "Bulk and Nanocatalysts Applications in Advanced Oxidation Processes" in *Oxidoreductase*, Eds. Mansour, M.A., IntechOpen, Rijeka, Croatia, 107–111.
- [3] Sathya, K., Nagarajan, K., Carlin Geor Malar, G., Rajalakshmi, S., and Raja Lakshmi, P., 2022, A comprehensive review on comparison among effluent treatment methods and modern methods

- of treatment of industrial wastewater effluent from different sources, *Appl. Water Sci.*, 12 (4), 70.
- [4] Sibhatu, A.K., Weldegebrerial, G.K., Sagadevan, S., Tran, N.N., and Hessel, V., 2022, Photocatalytic activity of CuO nanoparticles for organic and inorganic pollutants removal in wastewater remediation, *Chemosphere*, 300, 134623.
- [5] Zhang, S., Gu, P., Ma, R., Luo, C., Wen, T., Zhao, G., Cheng, W., and Wang, X., 2019, Recent developments in fabrication and structure regulation of visible-light-driven g-C₃N₄-based photocatalysts towards water purification: A critical review, *Catal. Today*, 335, 65–77.
- [6] Jiang, L., Yuan, X., Zeng, G., Wu, Z., Liang, J., Chen, X., Leng, L., Wang, H., and Wang, H., 2018, Metal-free efficient photocatalyst for stable visible-light photocatalytic degradation of refractory pollutant, *Appl. Catal., B*, 221, 715–725.
- [7] Chen, J., Abazari, R., Adegoke, K.A., Maxakato, N.W., Bello, O.S., Tahir, M., Tasleem, S., Sanati, S., Kirillov, A.M., and Zhou, Y., 2022, Metal–organic frameworks and derived materials as photocatalysts for water splitting and carbon dioxide reduction, *Coord. Chem. Rev.*, 469, 214664.
- [8] Akhoondi, A., Mirzaei, M., Nassar, M.Y., Sabaghian, Z., Hatami, F., and Yusuf, M., 2022, New strategies in the preparation of binary g-C₃N₄/MXene composites for visible-light-driven photocatalytic applications, *Synth. Sintering*, 2 (4), 151–169.
- [9] Kusworo, T.D., Kumoro, A.C., Aryanti, N., Hasbullah, H., Chaesarifa, D.R.S., Fauzan, M.D., and Dalanta, F., 2023, Developing a robust photocatalytic and antifouling performance of PVDF membrane using spinel NiFe₂O₄/GO photocatalyst for efficient industrial dye wastewater treatment, *J. Environ. Chem. Eng.*, 11 (2), 109449.
- [10] Oyewo, O.A., Elemike, E.E., Onwudiwe, D.C., and Onyango, M.S., 2020, Metal oxide-cellulose nanocomposites for the removal of toxic metals and dyes from wastewater, *Int. J. Biol. Macromol.*, 164, 2477–2496.
- [11] Weber, J.N., Minner-Meinen, R., Behnecke, M., Biedendieck, R., Hänsch, V.G., Hercher, T.W., Hertweck, C., van den Hout, L., Knüppel, L., Sivov, S., Schulze, J., Mendel, R.R., Hänsch, R., and Kaufholdt, D., 2023, Moonlighting *Arabidopsis* molybdate transporter 2 family and GSH-complex formation facilitate molybdenum homeostasis, *Commun. Biol.*, 6 (1), 801.
- [12] Pal, S., Sarkar, A., Satra, J., Mondal, P., Ray, P., Srivastava, D.N., Adhikary, B., and Show, B., 2022, Tetraphenylporphyrin decorated Bi₂MoO₆ nanocomposite: Its twin affinity of oxygen reduction reaction and electrochemical detection of 4-nitrophenol, *Inorg. Chem.*, 61 (44), 17402–17418.
- [13] Mohmoud, A., Rakass, S., Oudghiri Hassani, H., Kooli, F., Abboudi, M., and Ben Aoun, S., 2020, Iron molybdate Fe₂(MoO₄)₃ nanoparticles: Efficient sorbent for methylene blue dye removal from aqueous solutions, *Molecules*, 25 (21), 5100.
- [14] Wu, Y.Y., Song, B.Y., Zhang, X.F., Deng, Z.P., Huo, L.H., and Gao, S., 2021, Microtubular α-Fe₂O₃/Fe₂(MoO₄)₃ heterostructure derived from absorbent cotton for enhanced ppb-level H₂S gas-sensing performance, *J. Alloys Compd.*, 867, 158994.
- [15] Qiu, Y., Li, G., Zhou, H., Zhang, G., Guo, L., Guo, Z., Yang, R., Fan, Y., Wang, W., Du, Y., and Dang, F., 2023, Highly stable garnet Fe₂Mo₃O₁₂ cathode boosts the lithium–air battery performance featuring a polyhedral framework and cationic vacancy concentrated surface, *Adv. Sci.*, 10 (12), 2300482.
- [16] Nisar, J., Hassan, S., Khan, M.I., Iqbal, M., Nazir, A., Sharif, A., and Ahmed, E., 2020, Hetero-structured iron molybdate nanoparticles: Synthesis, characterization and photocatalytic application, *Int. J. Chem. Reactor Eng.*, 18 (2), 20190123.
- [17] Zhang, X., Liu, W., Gao, T., Cao, D., Che, X., Zhou, S., Shang, J., and Cheng, X., 2023, A novel iron molybdate photocatalyst with heterojunction-like band gap structure for organic pollutant degradation by activation of persulfate under simulated sunlight irradiation, *Environ. Sci. Pollut. Res.*, 30 (18), 53157–53176.
- [18] Seevakan, K., Manikandan, A., Devendran, P., Antony, S.A., and Alagesan, T., 2016, One-pot synthesis and characterization studies of iron

- molybdenum mixed metal oxide ($\text{Fe}_2(\text{MoO}_4)_3$) nanophotocatalysts, *Adv. Sci., Eng. Med.*, 8 (7), 566–572.
- [19] Zou, S., Luo, J., Lin, Z., Fu, P., and Chen, Z., 2018, Acetone gas sensor based on iron molybdate nanoparticles prepared by hydrothermal method with PVP as surfactant, *Mater. Res. Express*, 5 (12), 125013.
- [20] Liu, L., Zhao, J., Wang, S., Zhang, B., Yang, J., and Liu, H., 2023, Supercritical hydrothermal synthesis of nano-zirconia: Reaction path and crystallization mechanisms of different precursors, *E3S Web Conf.*, 406, 01025.
- [21] Obaid, A., and Ahmed, L., 2021, One-step hydrothermal synthesis of α - MoO_3 nano-belts with ultrasonic assist for incorporating TiO_2 as a nanocomposite, *Egypt. J. Chem.*, 64 (10), 5725–5734.
- [22] Mikhaylov, V., Krivoschapkina, E., Belyy, V., Isaenko, S., Zhukov, M., Gerasimov, E., and Krivoschapkin, P., 2019, Magnetic mesoporous catalytic and adsorption active $\text{Fe-Al}_2\text{O}_3$ films, *Microporous Mesoporous Mater.*, 284, 225–234.
- [23] Kılınç, D., and Şahin, Ö., 2019, Al_2O_3 based Co-Schiff base complex catalyst in hydrogen generation, *Int. J. Hydrogen Energy*, 44 (53), 28391–28401.
- [24] Abd Zaid, A.A., Ahmed, L.M., and Mohammad, R.K., 2022, Synthesis of inverse spinel nickel ferrite like-broccoli nanoparticle and thermodynamic study of photo-decolorization of alkali blue 4B dye, *J. Nanostruct.*, 12 (3), 697–710.
- [25] Sharma, A.K., and Lee, B.K., 2016, Surfactant-aided sol-gel synthesis of TiO_2 - MgO nanocomposite and their photocatalytic azo dye degradation activity, *J. Compos. Mater.*, 54 (12), 1561–1570.
- [26] Kadhim, H., Ahmed, L., and AL-Hachamii, M., 2022, Facile synthesis of spinel CoCr_2O_4 and its nanocomposite with ZrO_2 : Employing in photocatalytic decolorization of Fe(II) -(luminol-tyrosine) complex, *Egypt. J. Chem.*, 65 (1), 481–488.
- [27] Tsegaye, F., Tadesse, A.M., Teju, E., and Aschalew, M., 2020, Preparation and sorption property study of $\text{Fe}_3\text{O}_4/\text{Al}_2\text{O}_3/\text{ZrO}_2$ composite for the removal of cadmium, lead and chromium ions from aqueous solutions, *Bull. Chem. Soc. Ethiop.*, 34 (1), 105–121.
- [28] Saeed, S.I., Attol, D.H., Eesa, M.T., and Ahmed, L.M., 2023, Zinc oxide-mediated removal and photocatalytic treatment of direct orange 39 dye as a textile dye, *AIP Conf. Proc.*, 2414, 050021.
- [29] Jaafar, M.T., and Ahmed, L.M., 2020, Reduced the toxicity of acid black (nigrosine) dye by removal and photocatalytic activity of TiO_2 and studying the effect of pH, temperature, and the oxidant agents, *AIP Conf. Proc.*, 2290 (1), 030034.
- [30] Hussain, Z.A., Fakhri, F.H., Alesary, H.F., and Ahmed, L.M., 2020, ZnO based material as photocatalyst for treating the textile anthraquinone derivative dye (dispersive blue 26 dye): Removal and photocatalytic treatment, *J. Phys.: Conf. Ser.*, 1664 (1), 12064.
- [31] Saeed, S.I., Taresh, B.H., Ahmed, L.M., Haboob, Z.F., Hassan, S.A., and Jassim, A.A.A., 2021, Insight into the oxidant agents effect of removal and photo-decolorization of vitamin B_{12} solution in drug tablets using ZrO_2 , *J. Chem. Health Risks*, 11 (4), 393–402.
- [32] Ramachandran, K., Chidambaram, S., Baskaran, B., Muthukumarasamy, A., and Lawrence, J.B., 2017, Investigations on structural, optical and magnetic properties of solution-combustion-synthesized nanocrystalline iron molybdate, *Bull. Mater. Sci.*, 40 (1), 87–92.
- [33] Loomba, S., Khan, M., Haris, M., Mousavi, S., Zavabeti, A., Xu, K., Tadich, A., Thomsen, L., McConville, C.F., Li, Y., Walia, S., and Mahmood, N., 2023, Nitrogen-doped porous nickel molybdenum phosphide sheets for efficient seawater splitting, *Small*, 19 (18), 2207310.
- [34] Bekakria, H., Bendjefal, H., Djebli, A., Mamine, H., Metidji, T., and Benrdjem, Z., 2021, Heterogeneous sono-photo-Fenton degradation of methyl violet 10B using Fe_2O_3 - Al_2O_3 - Ga_2O_3 as a new photocatalyst, *Inorg. Nano-Met. Chem.*, 51 (12), 1759–1774.
- [35] Yin, C., Li, S., Liu, L., Huang, Q., Zhu, G., Yang, X., and Wang, S., 2022, Structure-tunable trivalent Fe-Al-based bimetallic organic frameworks for arsenic removal from contaminated water, *J. Mol. Liq.*, 346, 117101.

- [36] Casillas, J.E., Campa-Molina, J., Tzompantzi, F., Carbajal Arízaga, G.G., López-Gaona, A., Ulloa-Godínez, S., Cano, M.E., and Barrera, A., 2020, Photocatalytic degradation of diclofenac using $\text{Al}_2\text{O}_3\text{-Nd}_2\text{O}_3$ binary oxides prepared by the sol-gel method, *Materials*, 13 (6), 1345.
- [37] Ali, S., Ali, M., and Ahmed, L., 2021, Hybrid phosphotungstic acid-dopamine (PTA-DA) like-flower nanostructure synthesis as a furosemide drug delivery system and kinetic study of drug releasing, *Egypt. J. Chem.*, 64 (10), 5547–5553.
- [38] Hasan Tareh, B., Hadi Fakhri, F., and Ahmed, L.M., 2022, Synthesis and characterization of CuO/CeO_2 nanocomposites and investigation their photocatalytic activity, *J. Nanostruct.*, 12 (3), 563–570.
- [39] Sharifi, S., Yazdani, A., and Rahimi, K., 2020, Incremental substitution of Ni with Mn in NiFe_2O_4 to largely enhance its supercapacitance properties, *Sci. Rep.*, 10 (1), 10916.
- [40] Mursyalaat, V., Variani, V.I., Arsyad, W.O.S., and Firihi, M.Z., 2023, The development of program for calculating the band gap energy of semiconductor material based on UV-vis spectrum using Delphi 7.0., *J. Phys.: Conf. Ser.*, 2498 (1), 012042.
- [41] Yuniar, Y., Agustina, T., Faizal, M., and Hariani, P.L., 2023, Synthesis and characterization of $\text{ZnO/MnFe}_2\text{O}_4$ nanocomposites for degrading cationic dyes, *J. Ecol. Eng.*, 24 (4) 252–263.
- [42] Hariani, P.L., Said, M., Salni, S., Aprianti, N., and Naibaho, Y.A.L.R., 2021, High efficient photocatalytic degradation of methyl orange dye in an aqueous solution by $\text{CoFe}_2\text{O}_4\text{-SiO}_2\text{-TiO}_2$ magnetic catalyst, *J. Ecol. Eng.*, 23 (1), 118–128.
- [43] Kefeni, K.K., and Mamba, B.B., 2020, Photocatalytic application of spinel ferrite nanoparticles and nanocomposites in wastewater treatment: Review, *Sustainable Mater. Technol.*, 23, e00140.
- [44] Navajas, A., Reyero, I., Jiménez-Barrera, E., Romero-Sarria, F., Llorca, J., and Gandía, L.M., 2020, Catalytic performance of bulk and Al_2O_3 -supported molybdenum oxide for the production of biodiesel from oil with high free fatty acids content, *Catalysts*, 10 (2), 158.
- [45] Singh, B., Singh, P., Siddiqui, S., Singh, D., and Gupta, M., 2022, Wastewater treatment using Fe-doped perovskite manganites by photocatalytic degradation of methyl orange, crystal violet and indigo carmine dyes in tungsten bulb/sunlight, *J. Rare Earths*, 41 (9), 1311–1322.
- [46] Hossain, M.S., Tuntun, S.M., Bahadur, N.M., and Ahmed, S., 2022, Enhancement of photocatalytic efficacy by exploiting copper doping in nano-hydroxyapatite for degradation of Congo red dye, *RSC Adv.*, 12 (52), 34080–34094.
- [47] Wang, L., Deng, J., Jiang, M., Zhen, C., Li, F., Li, S., Bai, S., Zhang, X., and Zhu, W., 2023, Arene-perfluoroarene interactions in molecular cocrystals for enhanced photocatalytic activity, *J. Mater. Chem. A*, 11 (21), 11235–11244.
- [48] Pavel, M., Anastasescu, C., State, R.N., Vasile, A., Papa, F., and Balint, I., 2023, Photocatalytic degradation of organic and inorganic pollutants to harmless end products: Assessment of practical application potential for water and air cleaning, *Catalysts*, 13 (2), 380.
- [49] Singh, M., Kumar, A., and Krishnan, V., 2020, Influence of different bismuth oxyhalides on the photocatalytic activity of graphitic carbon nitride: A comparative study under natural sunlight, *Mater. Adv.*, 1 (5), 1262–1272.
- [50] Ahmed, S., 2004. Photo electrochemical study of ferrioxalate actinometry at a glassy carbon electrode, *J. Photochem. Photobiol., A*, 161 (2-3), 151–154.
- [51] Kamran, M., Morsy, M., Kandiel, T., and Iali, W., 2022, Semi-automated EPR system for direct monitoring the photocatalytic activity of TiO_2 suspension using TEMPOL model compound, *Photochem. Photobiol. Sci.*, 21 (12), 2071–2083.
- [52] Megatiff, L., Dillert, R., and Bahnemann, D.W., 2020, Determination of the quantum yield of a heterogeneous photocatalytic reaction employing a black body photoreactor, *Catal. Today*, 355, 698–703.
- [53] Qureshi, M., and Takanabe, K., 2017, Insights on measuring and reporting heterogeneous

- photocatalysis: Efficiency definitions and setup examples, *Chem. Mater.*, 29 (1), 158–167.
- [54] Ahmed, L.M., Saaed, S.I., and Marhoon, A.A., 2018, Effect of oxidation agents on photo-decolorization of vitamin B₁₂ in the presence of ZnO/UV-A system, *Indones. J. Chem.*, 18 (2), 272–278.
- [55] Cardoso, I.M.F., Cardoso, R.M.F., and da Silva, J.C.G.E., 2021, Advanced oxidation processes coupled with nanomaterials for water treatment, *Nanomaterials*, 11 (8), 2045.
- [56] Putri, R.A., Safni, S., Jamarun, N., Septiani, U., Kim, M.K., and Zoh, K., 2019, Kinetics studies on photodegradation of methyl orange in the presence of C-N-codoped TiO₂ catalyst, *Egypt. J. Chem.*, 62 (Part 2), 563–575.
- [57] Kazm, K.H., and Najim, S.T., 2022, Study kinetic reaction and removal of indigo carmine dye in aqueous solutions by direct electrochemical oxidation, *IOP Conf. Ser.: Earth Environ. Sci.*, 1002 (1), 012005.
- [58] Ortiz, E., Gómez-Chávez, V., Cortés-Romero, C.M., Solís, H., Ruiz-Ramos, R., and Loera-Serna, S., 2016, Degradation of indigo carmine using advanced oxidation processes: Synergy effects and toxicological study, *J. Environ. Prot.*, 7 (12), 1693–1706.
- [59] Zaouak, A., Noomen, A., and Jelassi, H., 2018, Gamma-radiation induced decolorization and degradation on aqueous solutions of Indigo Carmine dye, *J. Radioanal. Nucl. Chem.*, 317 (1), 37–44.